

Effects of the stellar wind on the Ly-alpha transit of close-in planets

S. Carolan,¹★ A. A. Vidotto,¹ C. Villarreal D’Angelo,^{2,1} G. Hazra¹

¹*School of Physics, Trinity College Dublin, College Green, Dublin 2, Ireland*

²*Observatorio Astronómico de Córdoba - Universidad Nacional de Córdoba. Laprida 854, X5000BGR. Córdoba, Argentina*

Accepted XXX. Received YYY; in original form ZZZ

ABSTRACT

We use 3D hydrodynamics simulations followed by synthetic line profile calculations to examine the effect increasing the strength of the stellar wind has on observed Ly- α transits of a Hot Jupiter (HJ) and a Warm Neptune (WN). We find that increasing the stellar wind mass-loss rate from 0 (no wind) to 100 times the solar mass-loss rate value causes reduced atmospheric escape in both planets (a reduction of 65% and 40% for the HJ and WN, respectively, compared to the ‘no wind’ case). For weaker stellar winds (lower ram pressure), the reduction in planetary escape rate is very small. However, as the stellar wind becomes stronger, the interaction happens deeper in the planetary atmosphere and, once this interaction occurs below the sonic surface of the planetary outflow, further reduction in evaporation rates is seen. We classify these regimes in terms of the geometry of the planetary sonic surface. “Closed” refers to scenarios where the sonic surface is undisturbed, while “open” refers to those where the surface is disrupted. We find that the change in stellar wind strength affects the Ly- α transit in a non-linear way (note that here we do not include charge-exchange processes). Although little change is seen in planetary escape rates ($\simeq 5.5 \times 10^{11}$ g/s) in the closed to partially open regimes, the Ly- α absorption (sum of the blue [-300, -40 km/s] & red [40, 300 km/s] wings) changes from 21% to 6% as the stellar wind mass-loss rate is increased in the HJ set of simulations. For the WN simulations, escape rates of $\simeq 6.5 \times 10^{10}$ g/s can cause transit absorptions that vary from 8.8% to 3.7%, depending on the stellar wind strength. We conclude that the same atmospheric escape rate can produce a range of absorptions depending on the stellar wind and that neglecting this in the interpretation of Ly- α transits can lead to underestimation of planetary escape rates.

Key words: planet-star interactions – planets and satellites: atmospheres – hydrodynamics – stars: winds and outflows

1 INTRODUCTION

Close-in exoplanets experience high levels of irradiation from their host stars, causing a substantial amount of photoevaporation of their atmospheres (Lammer et al. 2003; Baraffe et al. 2004; Yelle 2004). The amount of atmospheric escape determines the lifespan of a planet’s atmosphere (e.g., Johnstone et al. 2015; Kubyshkina et al. 2020), which is a key contributor to planetary habitability (Lingam & Loeb 2018; Dong et al. 2018), and is thought to shape the observed mass-radius distribution of close-in exoplanets (Kurokawa & Nakamoto 2014; Owen & Lai 2018; Berger et al. 2020). Additionally, atmospheric escape is believed to shape the period-radius distribution of close-in exoplanets, giving rise to the “evaporation desert” and the “radius valley”. The evaporation desert, also known as the Neptunian desert, affects gas giants in short orbit (Mazeh et al. 2016). The radius valley is an under-population of exoplanets with radius between 1.5 and 2.0 Earth radii and orbital periods lower than about 100 days (Beaugé & Nesvorný 2013; Fulton et al. 2017). More direct observational signatures of atmospheric escape have

been found in transmission spectroscopic transits of a few planets, such as HD209458b (Vidal-Madjar et al. 2003), HD189733b (Lecavelier Des Etangs et al. 2010; Lecavelier des Etangs et al. 2012; Jensen et al. 2012; Ben-Jaffel & Ballester 2013), GJ436b (Kulow et al. 2014; Ehrenreich et al. 2015), GJ3470b (Bourrier et al. 2018) and some others. These observations are often done in Ly- α line, where absorption is a consequence of neutral hydrogen leaving the planet due to the outflow generated by high energy radiation from the host star.

Once the planetary atmosphere expands and escapes, it interacts with the stellar wind, which shapes the geometry of the escaping atmosphere. This interaction can create different structures in the escaping atmosphere, such as a comet-like tail, trailing behind the planet, and a stream of material oriented ahead of the planet’s orbit and towards the star. The size and presence of these structures depend on a few key properties in the system, such as the orbital velocity, the ram pressure of the stellar wind, and tidal forces exerted by the star (Matsakos et al. 2015; Pillitteri et al. 2015; Shaikhislamov et al. 2016). For example, if the stellar wind is weak and the tidal forces are strong, a stream of planetary material can be created towards the star. If the stellar wind is strong, the orientation

★ E-mail: carolast@tcd.ie

of the comet-like tail can become more aligned with the star-planet line. These different structures can be detected in Ly- α , as they can contain a significant portion of neutral hydrogen. Because these structures are not spherically symmetric, they cause asymmetries in the transit light curve (e.g., an early ingress or late egress), and also affect the line profile (larger absorption in the blue and/or red wings of the line) (Vidal-Madjar et al. 2003; Lecavelier des Etangs et al. 2012; Kulow et al. 2014; Ehrenreich et al. 2015; Bourrier et al. 2018).

Using simulations, we can model the interactions between the stellar and planetary outflows, gaining key insights into the characteristics of the system. In the present work, we focus more specifically on the role of the stellar wind on the interaction with the escaping atmosphere and in particular whether the stellar wind can affect the amount of planetary escape. One crucial point in the theory of astrophysical flows, such as stellar winds and accretion disks, is the presence of ‘critical points’ (e.g. Parker 1958; Weber & Davis 1967). In the case of hydrodynamic outflows, such as the escaping atmospheres of close-in giants, one important critical point is the sonic point, which represents the location beyond which the planetary outflow becomes super-sonic. Planetary atmospheric escape models have suggested that the position of the sonic point (or surface, in the case of 3D geometries) in relation to the position where the interaction with the stellar wind happens, can act to reduce planetary escape rate (Christie et al. 2016; Vidotto & Cleary 2020). It has been suggested that if the stellar wind interacts with the super-sonic escaping atmosphere, the information cannot propagate upstream and it does not affect the inner regions of the planetary outflow. However, if this interaction occurs where the escaping atmosphere is sub-sonic, the inner outflow can be altered and therefore the escape rate can be affected (Vidotto & Cleary 2020). In the latter scenario, the stellar wind would act to confine the planetary outflow and reduce/prevent their escape (Christie et al. 2016).

Although an increase body of work on the 3D interaction between planetary atmospheres and stellar winds has become available recently (Bisikalo et al. 2013; Shaikhislamov et al. 2016; Schneiter et al. 2016; Carroll-Nellenback et al. 2017; Villarreal D’Angelo et al. 2018; McCann et al. 2019; Khodachenko et al. 2019; Esquivel et al. 2019; Debrecht et al. 2020, Villarreal D’Angelo et al. Submitted), the effect of stellar wind ‘confinement’ of planetary atmospheres has not yet been studied in 3D. For that, the interaction must occur within the sonic surface of the planetary outflow, and to the best of our knowledge, the aforementioned 3D studies have focused on the interaction that happens when the planetary outflow has already reached super-sonic speeds. To best model the confinement, the planetary outflow must be launched from the surface of the planet, as the inner regions of the planetary outflow must be examined in order to accurately quantify changes in the escape rate. This requires high resolution close to the planet, in which case a planet-centric single body model is therefore preferred (‘local’ simulations), as opposed to ‘global’ models that incorporate both the star and the planet in the numerical grid.

In this work we perform 3D local hydrodynamic simulations of atmospheric escape in close-in exoplanets, including the interaction with the stellar wind. We vary the strength of the stellar wind to investigate the effects it has on confining the outflowing atmosphere and on the atmospheric escape rate. We chose two exoplanetary systems (shown in figure 1, similar to HD209458b but orbiting a more active star and GJ3470b) to represent typical close-in gas giants. The details of our 3D model are discussed in section 2.2, with the results of these models presented in section 3. We compute the synthetic observations in Ly- α transits in section 4, and we show

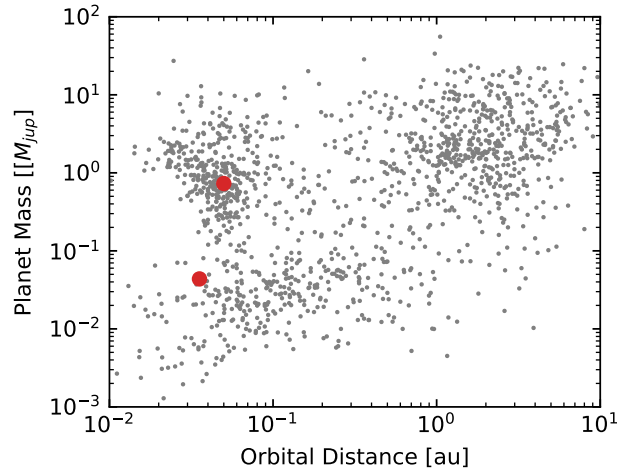


Figure 1. The masses vs orbital semi-major axis of all confirmed exoplanets are marked in grey (exoplanetarchive.ipac.caltech.edu). The red points mark the positions of the two planets examined in this work, they were chosen to have characteristics similar to GJ3470b, and HD209458b but orbiting a more active star.

that properly accounting for the presence of the stellar wind can affect the interpretation of spectroscopic transits. In particular, not including the stellar wind interaction can lead to an underestimation of atmospheric escape rates detected. A discussion of our results is shown in section 5 and we present our conclusions in section 6.

2 3D MODELLING OF THE INTERACTION BETWEEN THE STELLAR WIND AND PLANETARY ATMOSPHERIC ESCAPE

To model the interaction between the stellar wind and the escaping atmosphere, we use two numerical setups. Firstly, we run 1D radiation hydrodynamic simulations to simulate the photoevaporation of the planetary atmosphere. This yields an escape rate and velocity structure for a given atmosphere. These are then used to inform our 3D isothermal simulations, constraining the two free parameters: the base density and temperature of the outflowing atmosphere. Below, we detail our 1D radiation hydrodynamic model and 3D hydrodynamic model.

2.1 1D Model

Here, we briefly present the main characteristics of our 1D radiation hydrodynamics calculation, and refer the reader to Allan & Vidotto (2019) or Murray-Clay et al. (2009) for further details. This model treats the escaping atmosphere as a fluid. As well as the standard conservation of mass and momentum equations (discussed in section 2.2) this model solves an energy equation which contains additional heating/cooling terms to consider heating from photoionisation and Ly- α cooling (in the 1D model we do not include the Coriolis effect, and set $\gamma = 5/3$). This model also solves an equation of ionisation balance:

$$\frac{n_n F_{\text{EUVE}} e^{-\tau} \sigma_{\nu_0}}{e_{\text{in}}} = n_p^2 \alpha_{\text{rec}} + \frac{1}{r^2} \frac{d}{dr} (r^2 n_p u), \quad (1)$$

where n_n and n_p are the number densities of neutral and ionised

hydrogen, F_{EUV} is the EUV flux received by the planet, τ is the optical depth to ionising photons, σ_{v_0} is the cross section for the ionisation of hydrogen, and α_{rec} is the radiative recombination coefficient of hydrogen ions. This model assumes that the incoming EUV flux is concentrated at an energy of $e_{\text{in}} = 20$ eV (Murray-Clay et al. 2009).

This model takes the planetary parameters (table 1) as input, as well as the EUV flux from the host star: for the hot Jupiter, we used $L_{\text{EUV,HJ}} = 2.06 \times 10^{-5} L_{\odot}$, (chosen to be 25 times larger than that assumed in Murray-Clay et al. 2009) and for the warm Neptune, we used $L_{\text{EUV,WN}} = 3.73 \times 10^{-6} L_{\odot}$ (Bourrier et al. 2018). As a result, this yields an escape rate, as well as the velocity and ionisation fraction ($f_{\text{ion}} = n_p / (n_p + n_n)$) as a function of distance. With this information, we can constrain the two free parameters of the 3D isothermal model: the base density and temperature at the planetary radius (inner boundary). A unique temperature is chosen such that the velocity structure in 3D best matches the velocity structure from the 1D model, seen in figure 2. Similarly, the base density in the 3D simulations is adjusted, so that it and the matched velocity structure reproduce the escape rates resultant from the 1D model (\dot{m}_0 in table 1). By matching the velocity structure and escape rate, we ensure that the ram pressure of the escaping atmospheres in our 3D simulations without a stellar wind is close to that of the 1D model. We can then inject a stellar wind to examine the interaction between the stellar and planetary outflows, having vastly saved computational time by informing our 3D model with the 1D model.

2.2 Setup of our 3D models

To investigate the effects of the stellar wind on the reduction of atmospheric escape rates, we simulate the environments around close-in exoplanets using the Space Weather Modelling Framework (SWMF, Tóth et al. 2005). SWMF has previously been used to study, e.g., various solar system objects (Sternborg et al. 2011; Ma et al. 2013; Jia et al. 2015; Jia & Kivelson 2016; Carolan et al. 2019), the solar wind (e.g. Manchester et al. 2004; van der Holst et al. 2011) and stellar winds (e.g. Vidotto et al. 2018; Kavanagh et al. 2019). For our investigation, we create a new user implementation to SWMF. This involves the design of new inner and outer boundary conditions, and additional source terms in the hydrodynamic equations, all of which are outlined below.

We model the stellar wind and escaping atmosphere as isothermal winds (Parker 1958), we do not include the effects of magnetic fields (this will be the topic of a future study), and consider only hydrogen in our simulations. There are two unknowns in the Parker wind model, the base density and temperature. To guide the selection of temperature and density of the planetary outflow, we use information from our 1D model (Allan & Vidotto 2019, see section 2.1). For the stellar winds we chose temperatures appropriate for stars hosting close-in exoplanets (see table 1), and vary the base density to control the stellar mass loss rate.

Our 3D simulations are Cartesian and solve for 5 parameters in the corotating frame: the mass density (ρ), velocity (u_x, u_y, u_z) and thermal pressure (P_T). These are found through iteratively solving a set of ideal hydrodynamic equations that includes the mass conservation equation

$$\frac{\partial \rho}{\partial t} + \nabla \cdot (\rho \vec{u}) = 0, \quad (2)$$

the momentum conservation equation

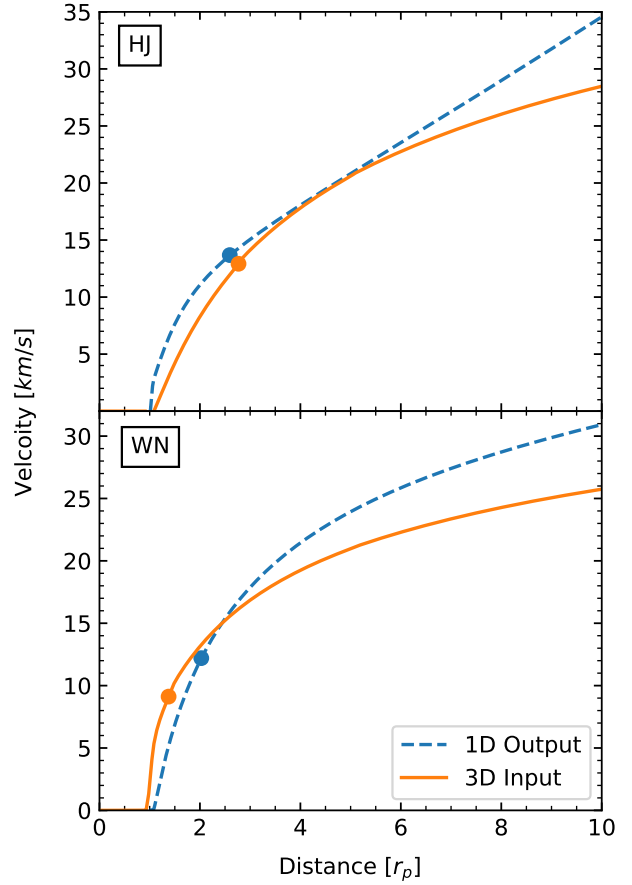


Figure 2. Velocity vs distance for the escaping atmosphere of both of our models. The dashed blue line shows the output of the 1D model, while the solid orange shows the initial condition we implement in our isothermal 3D model. The base density in the 3D model is then adjusted so that the same escape rate is obtained in both the 1D and 3D models. The circles mark the position of the sonic point in each model.

$$\frac{\partial(\rho \vec{u})}{\partial t} + \nabla \cdot [\rho \vec{u} \vec{u} + P_T I] = \rho \left(\vec{g} - \frac{GM_*}{(r-a)^2} \hat{R} - \vec{\Omega} \times (\vec{\Omega} \times \vec{R}) - 2(\vec{\Omega} \times \vec{u}) \right), \quad (3)$$

and energy conservation equation

$$\frac{\partial \epsilon}{\partial t} + \nabla \cdot [\vec{u}(\epsilon + P_T)] = \rho \left(\vec{g} - \frac{GM_*}{(r-a)^2} \hat{R} - \vec{\Omega} \times (\vec{\Omega} \times \vec{R}) \right) \cdot \vec{u}, \quad (4)$$

where I is the identity matrix, \vec{g} the acceleration due to the planet's gravity, G the gravitational constant, and M_* is the mass of the star. \vec{r} is the position vector relative to the planet, \vec{a} the position of the star relative to the planet, $\vec{\Omega}$ the orbital rotation rate, and \vec{R} is the position vector relative to the star, as shown in figure 3. The total energy density ϵ is given by:

$$\epsilon = \frac{\rho u^2}{2} + \frac{P_T}{\gamma - 1}. \quad (5)$$

where the thermal pressure is $P_T = \rho k_B T / (\mu m_p)$, where k_B is the Boltzmann constant, μ is the mean mass per particle and m_p is the

Table 1. The planet and stellar properties in each set of models. M_p and r_p describe the planet's mass and radius, a is the orbital distance. \dot{m}_0 is the planetary atmospheric escape rate (with no stellar wind), u_{kep} is the Keplerian velocity of the system. T_p and $n_{0,p}$ are the temperature and base density of the planet's outflowing atmosphere in the 3D model that were found to best match the results of the 1D model. M_* , R_* and T_* describe the stellar mass, radius and stellar wind temperature, respectively, while the stellar wind radial velocity at each planet's orbital distance is given as u_{local} . Finally, $F_{\text{EUV}}(a)$ is the EUV flux at the planet's orbital distance.

Planet	M_p [M_{Jup}]	r_p [R_{Jup}]	a [au]	\dot{m}_0 [10^{10} g/s]	u_{kep} [km/s]	T_p [10^4 K]	$n_{0,p}$ [10^9 cm $^{-3}$]	M_* [M_{\odot}]	R_* [R_{\odot}]	T_* [10^6 K]	u_{local} [km/s]	$F_{\text{EUV}}(a)$ [erg/cm 2 /s]
HJ	0.7	1.4	0.050	58	147	1	3.86	1.00	1.00	2	400	1.12×10^4
WN	0.04	0.41	0.036	6.5	116	0.5	3.03	0.54	0.55	1	240	3.92×10^3

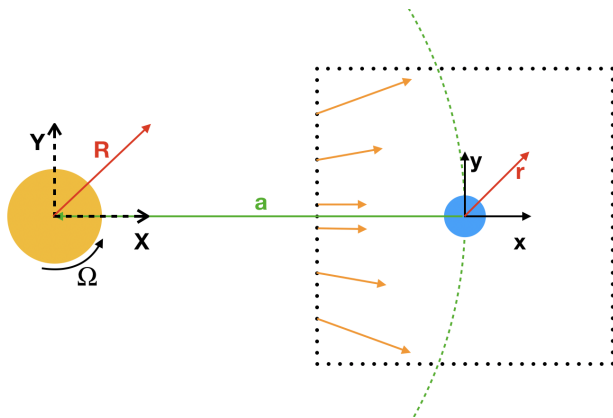


Figure 3. The coordinate system used in our simulations (not to scale). The orange circle represents the star, while the blue shows the planet. The uppercase letters show the direction of vectors in the stellar system, while the lowercase letters show the axes in the planetary system. The black dotted square represents our computational grid, while the green dashed line shows the path of the planet's orbit. The orange arrows represent the changing direction and magnitude of the stellar wind velocity as it enters the simulation grid. Note that, because of the close distance to the star, we can not assume that the stellar wind has a plane-parallel injection, as is usually assumed in simulations of planets that orbit far from their host stars (e.g. Carolan et al. 2019).

mass of the proton. Given that our calculations are done in the non-inertial frame, where the planet is fixed at the origin, we include the non-inertial forces in the hydrodynamic equations as source terms. These terms are shown in the right-hand side of Equations (3) and (4) and they are: the Coriolis force ($-2\rho(\vec{\Omega} \times \vec{u})$), the centrifugal force and stellar gravity that combined give rise to the ‘tidal force’ ($-\rho(GM_*/(r-a)^2)\vec{R} - \rho\vec{\Omega} \times (\vec{\Omega} \times \vec{R})$).

Our simulations model the isothermal flow of ionised hydrogen around the planet, similar to the work of Bisikalo et al. (2013); Carroll-Nellenback et al. (2017). To achieve this, we set the mean mass per particle $\mu = 0.5 m_p$ and the polytropic index $\gamma \approx 1$, which ensures a constant temperature in the outflow. The exoplanet is placed at the origin of a rectangular grid ($x, y = [-50, 50 r_p]$, $z = [-32, 32 r_p]$, where r_p is the radius of the planet) as seen in figures 3 and 4. For simplicity we chose the planet to be tidally locked to the star, such that the star is always located at negative x , while the planet orbits in the positive y direction. z constructs the right-handed system. This approach is justified, given that many close-in exoplanets are thought to be tidally locked to their host star (Kasting et al. 1993; Edson et al. 2011). Our simulations contain 16 million cells and have a minimum cell size of $1/16 r_p$ within a radius of $5 r_p$, which gradually decreases towards the edge of

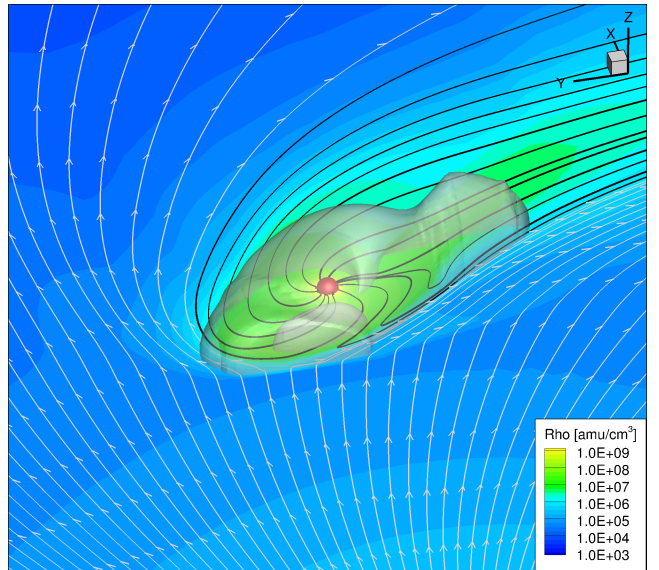


Figure 4. A 3D view of the HJ model for a stellar mass-loss rate of $10 M_{\odot}$. The colour shows the density in the orbital plane. The gray surface marks the sonic surface around the planet. The grey streamlines show the flow of the stellar wind in the grid, while the black lines trace the escaping atmosphere of the planet.

the grid. We found increasing the maximum resolution of these simulations showed no significant change in the results.

The inner boundary is placed at the surface of the planet ($r = 1 r_p$), where we keep the base density $n_{0,p}$ and temperature T_p of the escaping atmosphere fixed throughout the simulations. The base values adopted for each of the modelled planets are shown in table 1. These values give rise to an escape rate \dot{m}_0 , which matches that found in the 1D model. Finally, we assume the velocity of the outflow to be reflective in the non-inertial frame, effectively setting the inner velocity to ≈ 0 .

The simulation box has six outer boundaries, one for each face of the rectangular grid. The stellar wind is injected to the grid at the negative x boundary. The physical properties of the stellar wind are found by modelling an isothermal 1D stellar wind model at a given temperature T_* (Parker 1958). The mass-loss rate (\dot{M}) is a free parameter of the stellar wind model, that we vary in our study to change the strength of the incoming stellar wind. For a given \dot{M} and T_* , the 1D solution provides the velocity and density of the stellar wind at every point on the face of the negative x boundary. We orient the stellar wind to flow radially away from the star, but as it is injected in the simulation domain, we account for the Coriolis velocity ($-\vec{\Omega} \times \vec{R}$) to convert to the planet's reference frame.

On all remaining faces of our rectangular grid, we use an inflow limiting boundary condition, similar to McCann et al. (2019). This means that the outer boundary applies normal floating boundary conditions to cells where the velocity is directed outward, but set the momenta to 0 if the velocity component is directed inward. This is necessary as the Coriolis force can bend the flow of material close to the outer boundaries, such that uncontrolled inflows are generated when normal floating outflow conditions are applied. This can cause numerical issues such that no steady state solution is attainable, especially in smaller computational grids. The inflow limiting condition prevent this, ensuring that only the stellar wind is being injected into our grid.

3 SIMULATIONS OF REDUCED ATMOSPHERIC ESCAPE IN CLOSE-IN PLANETS

Using this computational setup we model two exoplanets for a range of stellar wind conditions: a Hot Jupiter similar to HD209458b but orbiting a more active solar-like star (labelled “HJ”); and a Warm Neptune similar to GJ3470b (labelled “WN”) which orbits an M dwarf. The relevant parameters used in the HJ and WN models are also provided in table 1.

For each planet we compute 13 and 14 models respectively, increasing the stellar wind mass-loss rate from 0 to 100 times the solar mass-loss rate ($\dot{M}_\odot = 2 \times 10^{-14} M_\odot/\text{yr}$). Given that it is difficult to measure the winds of cool dwarf stars, we chose this large range of stellar mass-loss rates to establish if and when neglecting the presence of the stellar wind as a contributing factor to signatures of atmospheric escape is appropriate. We note that this can only be achieved in multi-dimensional studies, as 1D models cannot account for the presence of a stellar wind. We chose to keep the temperatures of the isothermal stellar wind constant in each set ($T_{\star,\text{HJ}} = 2 \times 10^6 \text{ K}$, $T_{\star,\text{WN}} = 1 \times 10^6 \text{ K}$), retaining the same stellar wind velocity structure within each set of models. Varying the mass-loss rate, therefore, solely changes the stellar wind density. This setup allows us to investigate the effect that gradually increasing the stellar wind ram pressure ($\propto \dot{M} u_{\text{local}}$, where \dot{M} is the stellar wind mass loss rate, and u_{local} is the velocity of the stellar wind at the planet’s orbit) has on the planet’s escaping atmosphere. The density structure and velocity flow in the orbital plane of three models from each set are shown in figure 5. As we increase the stellar wind mass-loss rate we see the transition from type 2 / “weak” to the type 1 / “strong” scenarios shown by Matsakos et al. (2015) / McCann et al. (2019) respectively.

In the left panels of figure 5 we can see a large sonic surface created when the super-sonic stellar wind is shocked as it meets the super-sonic planetary outflow. As the ram pressure of the stellar wind increases this interaction happens closer to the planet. This confinement eventually affects the sonic surface of the escaping atmosphere, as seen in the changing white contour close to the planet from left to right panels in figure 5. The inner circular sonic surfaces in the left panels are unaffected (labelled “closed”). In the right panels the stellar wind has confined the outflow such that the sonic surface has been altered on all sides of the planet (labelled “open”). The middle panels show the transition between these two states, where the day-side sonic surface has changed, while the night-side surface remains largely unaffected.¹ Note that the inner

¹ The additional $M=1$ transition, in figure 5 is due to the fact that both the stellar and planetary winds are supersonic. As a result there are two shocks, one outer “bow shock” where the stellar wind is shocked, and an inner

Table 2. Summary of our simulation results. The stellar wind mass-loss rate (\dot{M}) is varied in each simulation, affecting the planetary atmospheric escape rate \dot{m} and Ly- α absorption at mid-transit computed in the blue [-300 to -40 km/s] plus red [40 to 300 km/s] wings (including the broad-band absorption due to the planetary disc). Here, the superscripts HJ and WN refer to the Hot Jupiter and Warm Neptune cases, respectively.

\dot{M} (HJ) (\dot{M}_\odot)	\dot{m}^{HJ} (10^{10} g/s)	ΔF^{HJ} (%)	\dot{M} (WN) (\dot{M}_\odot/yr)	\dot{m}^{WN} (10^{10} g/s)	ΔF^{WN} (%)
0	58	20.7	0	6.5	8.8
2	56	12.0	1	6.6	7.3
4	55	8.6	2	6.4	5.3
6	55	6.9	4	6.5	4.0
8	57	6.4	10	6.4	3.7
10	51	6.0	15	6.4	3.7
12	40	5.9	20	6.5	3.7
14	37	5.8	25	6.4	3.7
16	35	5.8	30	6.2	3.6
20	30	5.5	35	6.0	3.5
30	27	5.1	40	5.8	3.4
60	22	4.2	50	5.4	3.2
100	21	3.9	75	4.6	2.8
-	-	-	100	3.9	2.4

sonic surface of the WN planet is at $1.1 r_p$. Published models (eg. Villarreal D’Angelo submitted) of GJ436b, also a Warm Neptune, have shown that the $M = 1$ transition occurs farther out, where M is the mach number. The low position of the sonic point in our 3D models is due to our choice of temperature (see figure 2). We will come back to how a larger sonic surface would change our results when we further discuss the limitations of our model in section 5.2.

Previous models have shown that stellar wind confinement can affect the escape rate of the planets atmosphere (Vidotto & Cleary 2020; Christie et al. 2016). To investigate the difference in escape rate between our closed and open 3D models, we integrate the mass flux through concentric spheres around the planet, obtaining the atmospheric escape rate:

$$\dot{m} = \oint_A \rho \vec{u} \cdot d\vec{A}. \quad (6)$$

Table 2 shows a summary of the results of our simulations. The escape rate from each model is plotted in figure 6. Due to resolution, the escape rate can show small variations with distance from the planet, especially at the point where the stellar wind and escaping atmosphere meet. This small variation is quantified by the blue error bars in figure 6, which show one standard deviation from the mean escape rate in each model. Some models only reach a quasi-steady state solution, showing small periodic variability with increasing time step. For these models the maximum deviation is shown as a red error bar, while the average deviation over one period of the quasi-steady state variability is shown in blue. In both model sets, increasing the stellar wind mass-loss rate has reduced the atmospheric escape rate. For the HJ models, the escape rate has been reduced by 65% (from $5.8 \times 10^{11} \text{ g/s}$ to $2.1 \times 10^{11} \text{ g/s}$, see table 2). The WN models show a more gradual change, with a maximum reduction of 40% (from $6.5 \times 10^{10} \text{ g/s}$ to $3.9 \times 10^{10} \text{ g/s}$) over the range of stellar winds examined.

“termination shock” where the supersonic escaping atmosphere is shocked. This is similar to what is shown in models of the interaction between the heliosphere and the ISM (eg. Zank & Müller 2003), where instead it is the inner stellar wind and outer ISM forming two shockwaves.

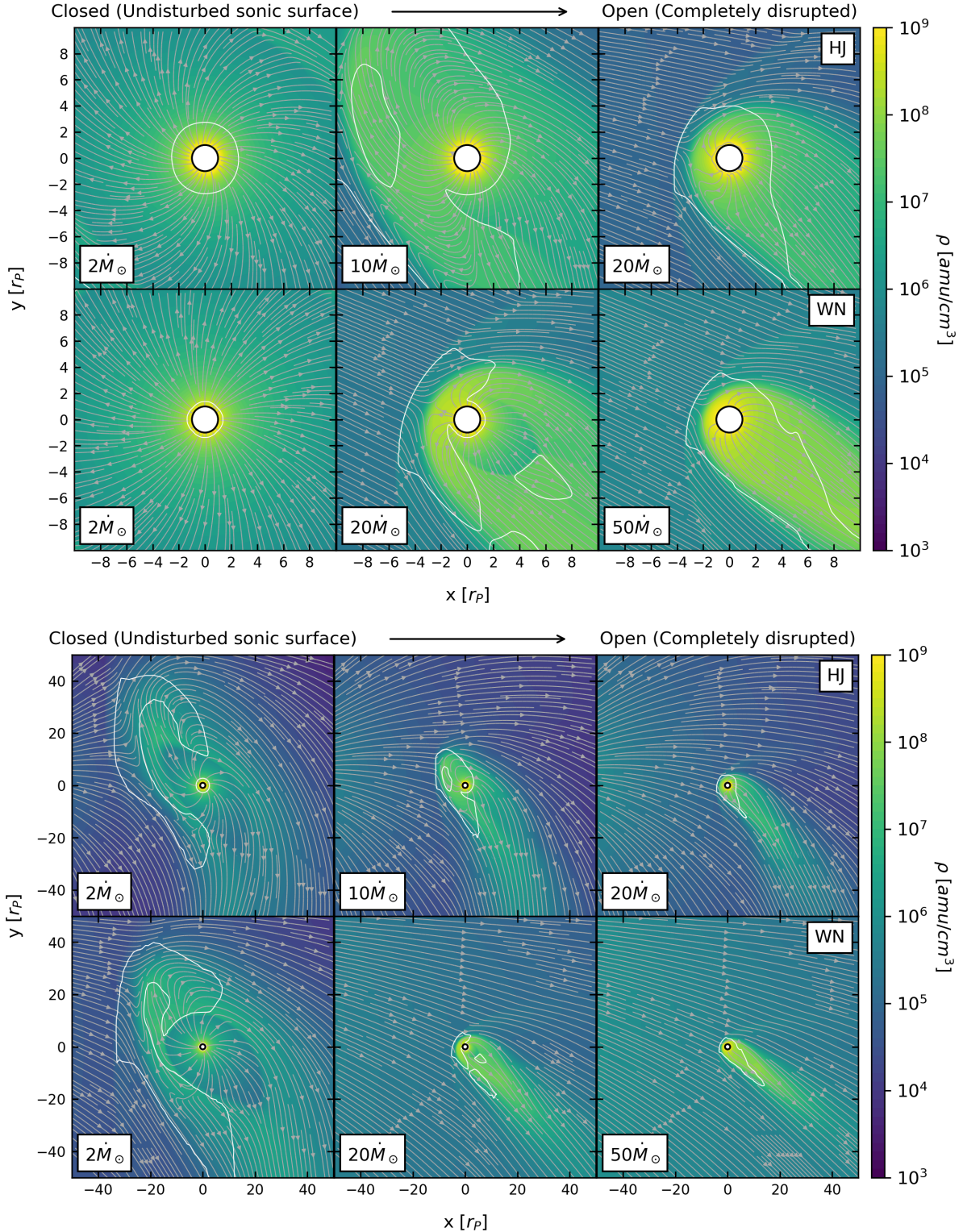


Figure 5. Top: The orbital slice of 3 Hot Jupiter (HJ, top) and 3 Warm Neptune (WN, bottom) models, chosen to illustrate transition from “closed” to “open” sonic surfaces for each planet. “Closed” refers to the scenarios where the inner (circular) sonic surface around the planet is not disturbed by the stellar wind. Contrary to that, “open” refers to the scenarios where this surface is disrupted. The planet is orbiting in the positive y direction, with the star at negative x. The colour shows the distribution of density around the planets, while the white contour marks a Mach number of 1, which shows the sonic surface around each planet. The streamlines trace the velocity of material in each model, in the planet’s reference frame. Bottom: A zoomed out version of this figure, showing the orbital plane from our grids. Here we can more clearly see the injection of the stellar wind from the negative x side of our grid, as well as the extension of material both ahead and behind the planet’s orbit.

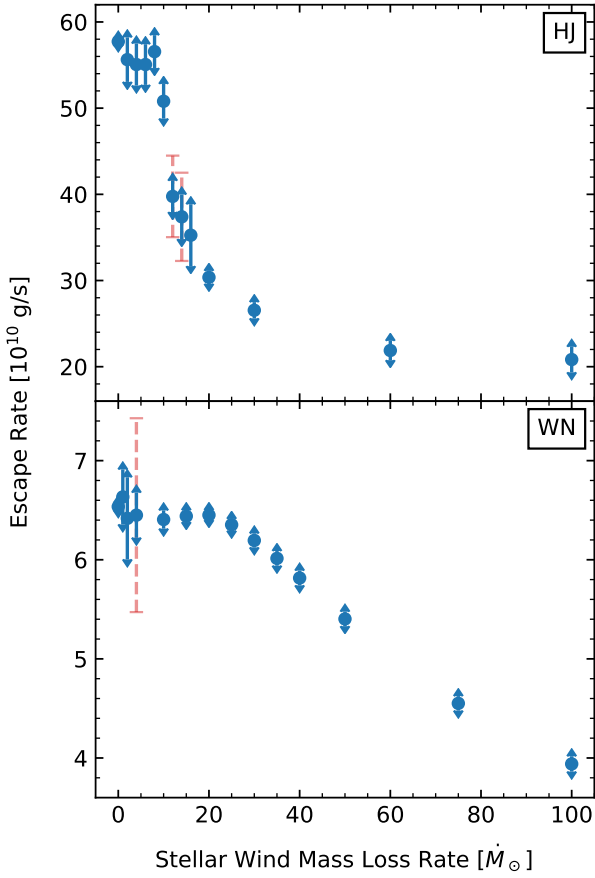


Figure 6. The variation of atmospheric escape rate with stellar mass-loss rate for each of our models. The points mark the mean escape rate, while the blue error bars illustrate one standard deviation from the mean. As some models reach a quasi-steady state solution, the average over several time steps is taken, and plotted in blue. For these models, the standard deviation at a single time step is shown in red.

As the stellar wind mass-loss rate increases, the escaping atmosphere is confined to a reduced volume around the planet, which is clearly visible from the velocity streamlines in figure 5 (left to right). This decelerates material on the day-side of the planet, redirecting it towards the planetary tail as seen in figure 5. As the flow of the escaping atmosphere is further confined, this deceleration occurs closer to the planet, where it eventually inhibits the dayside flow from reaching super-sonic speeds. As a result, the atmospheric escape rate is gradually reduced as the flow's sonic surface is further disrupted.

This change in escape rate occurs more suddenly in the HJ models than in the WN models as \dot{M} is increased. We propose this is related to the distance of the sonic point. In the closed HJ and WN models these are approximately $2.5 r_p$ and $1.1 r_p$ respectively. As a result the outflow in the WN models must be confined relatively closer to the planet in order for the sonic surface to be affected. This results in a more gradual reduction of atmospheric escape in the WN models, as a stronger stellar wind is required to further confine this outflow and open the sonic surface. In the HJ models, this is not the case. The change from closed to open geometries happens over a much shorter range of \dot{M} , as the sonic surface is relatively

further from the planet, and so can be more easily accessed by the stellar wind.

4 SYNTHETIC OBSERVATIONS: REDUCED LYMAN- α TRANSIT DEPTH BY STELLAR WIND CONFINEMENT

We use a ray tracing model to simulate the Ly- α line profile of each planet at mid transit. A full description of this model is outlined in Vidotto et al. (2018); Allan & Vidotto (2019). We further adapt this model to take our 3D grids as input. Given that the ray tracing model is constructed for an equally-spaced grid and calculations are done in the inertial reference frame, we interpolate our non-uniform 3D grid to contain 201 points equally-spaced in each dimension, describing the density, temperature, and line of sight velocity of the planetary material in the (observer's) inertial frame. Given that the stellar wind and the planetary outflow have very different temperatures, we separate planetary from stellar wind material by means of a temperature cutoff. To ensure we capture all the material escaping the planet, we use a temperature cutoff that is slightly higher than the temperature of the planetary outflow, ensuring that all the planetary material capable of absorbing in Ly- α is considered when producing the synthetic observations. Our current 3D model does not treat both the neutral and ionised portions of the planetary outflow, it simulates purely the ionised part ($\mu = 0.5$). Therefore, we estimate the neutral hydrogen density (n_n) from the ionisation balance equation solved self-consistently in the 1D escape model from Allan & Vidotto (2019), which tracks both the neutral and ionised density, as outlined in section 2.1. Our 3D model yields the density of ionised hydrogen (n_p) which can be used with the ionisation fraction from the 1D model (f_{ion}) to find the neutral density as follows:

$$n_n = n_p \frac{1 - f_{\text{ion}}}{f_{\text{ion}}} \quad (7)$$

Although this is not the most precise approach to calculate the neutral hydrogen density, this post-processing technique is a workaround adopted when the ionisation balance equation is not solved self-consistently with the hydrodynamics equations (similar approach has been used by Oklopčić & Hirata (2018) when calculating the population levels of helium, and by Lampón et al. (2020) when modelling helium in HD209458b's atmosphere). One limitation of this approach is that the 1D model computes the ionisation fraction along the star-planet line. Therefore, when we incorporate the ionisation fraction predicted in the 1D models in our 3D grid, the density of neutral material in the night side, or planetary tail, is not properly calculated. However, given that the inner regions of our 3D simulations are approximately spherically symmetric and contain most of the absorbing material, using the resultant ion fraction from the 1D model is an acceptable approximation for computing the synthetic observations.

Once the neutral density is estimated, the frequency ν dependent optical depth along the line of sight is given by:

$$\tau_\nu = \int n_n \sigma \phi_\nu dx, \quad (8)$$

where the observer is placed at positive x and ϕ_ν is the Voigt line profile function. The absorption cross section at line centre is $\sigma = \pi e^2 f / (m_e c)$, where $f = 0.416410$ is the oscillator strength for Ly- α , m_e is the mass of the electron, e is the electron charge and c is the speed of light. Using these, the fraction of transmitted intensity is given by:

$$\frac{I_\nu}{I_*} = e^{-\tau_\nu}. \quad (9)$$

Therefore, $1 - I_\nu/I_*$ represents the fraction of intensity that is absorbed by the planet's disc and atmosphere. We shoot 201×201 stellar rays through the grid. Integrating over all rays, and dividing by the flux of the star allows for the frequency-dependent transit depth (ΔF_ν) to be calculated:

$$\Delta F_\nu = \frac{\int \int (1 - e^{-\tau_\nu} dy dz)}{\pi R_*^2}. \quad (10)$$

For each of the models in the HJ and WN set, the transit depth as a function of velocity is shown in figure 7, and the integrated percentage absorption is given in table 2. As the Ly- α line centre is dominated by interstellar absorption and geocoronal emission, we omit the line centre $[-40, 40]$ km/s from these plots. In both model sets, the maximum transit depth decreases as the planetary outflow is further confined. This is due to the volume of absorbing planetary material around the planet decreasing as the escaping atmosphere is confined.

For most models, there is an obvious asymmetry in the line profile, with the blue wing showing more absorption than the red. In the low \dot{M} models, there is significant dayside (redshifted) outflow towards the star, similar to that seen by Matsakos et al. (2015) in their type 2 interaction, and in the "weak" stellar wind scenarios of McCann et al. (2019). As \dot{M} increases, this dayside stream is suppressed completely, as seen in figure 5. What remains is the planetary tail, containing mostly blue shifted material (type 1 in Matsakos et al. (2015); "strong" stellar wind in McCann et al. (2019)), leading to the line profile asymmetry we see in figure 7.

We quantify this asymmetry by integrating the modelled transit line profiles in figure 7 over velocity in the blue [-300, -40 km/s] and red [40, 300 km/s] wings. Note that our 3D model does not consider energetic neutral atoms (ENAs), and so the effect of these in the transit line profiles are not reflected in these calculations. For more discussion on this see section 5.2. The results of this are shown in figure 8. Note that even in the case with no stellar wind the line shows asymmetry due to the orbital motion and tidal forces. We can clearly see that in both models at low stellar mass-loss rates the absorption in the red wing dominates due to the significant dayside stream as mentioned above. As the stellar mass-loss rate is increased, the absorption in the blue wing begins to dominate as this dayside flow is further confined. This is a more sudden change in the WN model than with the HJ planet, as the HJ planet has a stronger outflow/higher escape rate. For both models the level of asymmetry is approximately constant within a certain range of stellar mass-loss rates. For the HJ models, the blue wing absorbs 1-2% more than the red from models between 10 and $30 M_\odot$. The WN models absorb roughly 0.25% more in the blue between 10 and $40 M_\odot$. Above these ranges the difference in absorption between the blue and red wing gradually decreases as the outflow becomes significantly more confined. For stellar wind mass-loss rates $< 10 M_\odot$, despite the percentage absorption of each wing changing significantly (approximately 10% in the HJ, 3% in WN) the atmospheric escape rate has not been affected as seen by the values on figure 8, and in figure 9. As mentioned in section 3, the stellar wind further confines the escaping planetary material, which in turn shapes the absorbing material around the planet. However for low stellar mass-loss rates the sonic surface of the atmospheric outflow is not yet affected, thus the escape rate remains unchanged.

We further investigate the total absorption (blue + red) rela-

tionship with the atmospheric escape rate in figure 9. The filled and open circles represent the results for the HJ and WN models, respectively. The stellar wind mass-loss rate is increased from right to left points, with the right-most point in each set being the one without the presence of a stellar wind (marked with an x). For each set of models, we see a region of our parameter space where, although the planetary escape rate is constant (marked with dotted lines), the transit absorption is not. As mentioned previously, this is due to stellar wind confinement, whereby the increasing ram pressure of the stellar wind confines absorbing material closer to the planet, therefore covering a decreased region on the stellar disc (Vidotto & Cleary 2020). In the HJ model set, a constant planetary escape rate of approximately $\dot{m}_{\text{HJ}} \simeq 5.5 \times 10^{11}$ g/s produces 6% to 21% absorption, depending on the stellar wind condition. For the WN planet, a constant planetary escape rate of $\dot{m}_{\text{WN}} \simeq 6.5 \times 10^{10}$ g/s produces 4% to 9% absorption. This reflects what is seen in figure 8, where the absorption of each wing has changed significantly, but the escape rate has not. As previously discussed in section 3, in the models showing absorption within the quoted ranges, the sonic surface remains intact (our 'closed' scenario), so the escape rate is unaffected by the changing stellar wind. Above a mass-loss rate of $10 M_\odot$ (or $20 M_\odot$ for the WN model), i.e., below an absorption of approximately 6% for the HJ models (or 4% for the WN models), the stellar wind begins to open the sonic surface, causing reduced atmospheric escape. In the range of WN models examined, the escape rate is reduced by approximately 40%, from 6.5×10^{10} to 4×10^{10} g/s, changing the total absorption by about 7%. For comparison, a similar 40% reduction in the HJ set, say, from 5.8×10^{11} to 3.3×10^{11} g/s, in escape rate occurs over a 15% range in total absorption.

5 DISCUSSION

5.1 Implications for interpreting Ly- α signatures

The results presented in section 4 emphasise the importance of considering the stellar wind when interpreting transit observations. For example, suppose that a planet similar to our HJ model is observed with 5.5% of absorption in the Ly- α line. In the presence of a stellar wind, we would interpret this observational result as being caused by a planetary outflow that has an intrinsic escape rate of $\sim 3 \times 10^{11}$ g/s (see Figure 9). However, had we not considered the presence of a stellar wind, we would have predicted a lower planetary escape rate to be able to reproduce this 5.5% observed transit absorption. This is because, without stellar wind confinement, the absorbing material can now occupy a greater volume around the planet, yielding the same percentage absorption for a lower escape rate. Therefore, given the degeneracy between planetary escape rates and stellar wind strengths for a same percentage absorption, we suggest that, in order to make a more accurate estimate of a planet's atmospheric escape rate, one should also consider the presence of a stellar wind.

Another consequence found in our study is that the stellar wind confinement can act to mask observational signatures of atmospheric escape in Ly- α . One instance of this could be with the sub-Neptune π Men c. The surprising lack of detection of Ly- α absorption led García Muñoz et al. (2020) to suggest a lack of hydrogen in the atmosphere of π Men c. If this is indeed the case, they proposed that further observations of heavier elements, such as OI and CII lines, could still reveal high atmospheric evaporation rate. An alternate explanation was proposed by Vidotto & Cleary (2020), who suggested that the atmosphere of π Men c could be

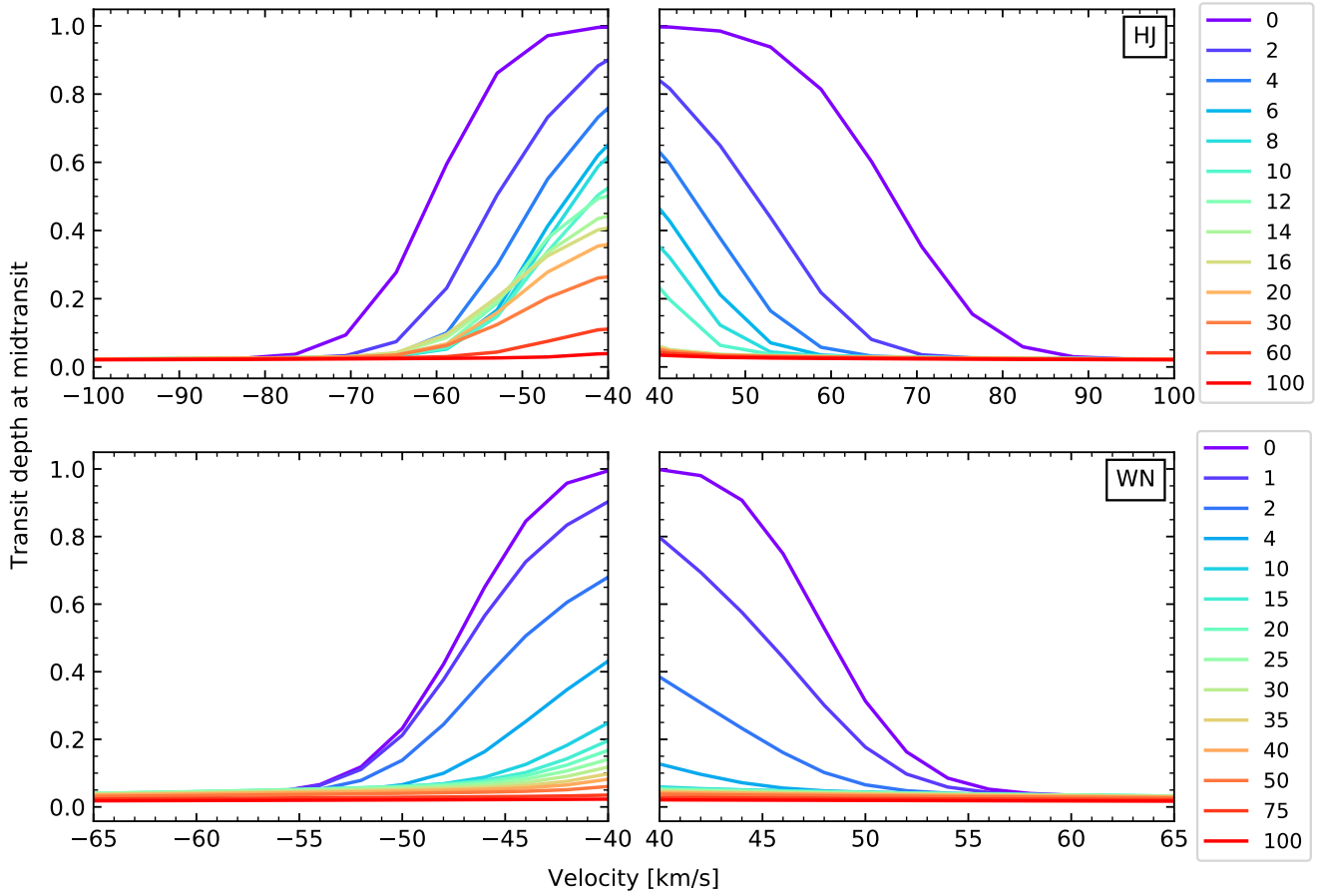


Figure 7. The blue (left) and red (right) wings of the in-transit Ly- α line profile (equation 10) for each of our HJ (top) and WN (bottom) models. The colour shows the variation of stellar mass-loss rate from 0 to $100 M_{\odot}$. As the line centre is contaminated by interstellar absorption and geocoronal emission, we ignore the velocity range of -40 to 40 km/s. Note how the transit absorption is larger in the red wing for low stellar \dot{M} and larger in the blue wing for high stellar \dot{M} .

hydrogen-rich, but would remain undetected if a significant reduction in escape was being caused by the stellar wind. They proposed that this could take place in π Men c as they found that the stellar wind interaction happened in the sub-sonic part of the planetary outflow.

As we showed here, the position where the interaction happens depends on the strength of the stellar wind and on the properties of the escaping atmosphere. One important parameter in atmospheric modeling is the stellar high-energy flux that is deposited on the planet's atmosphere. In Vidotto & Cleary (2020), they assumed a flux of $1340 \text{ erg cm}^{-2}\text{s}^{-1}$ and a stellar wind mass-loss rate of $1 M_{\odot}$ for π Men c. To investigate this further, Shaikhislamov et al. (2020) performed 3D simulations of the stellar wind of π Men c and, using a similar stellar wind condition and high-energy flux than those assumed in Vidotto & Cleary (2020), confirmed that the interaction was taking place in the sub-sonic regime, but did not obtain a significant reduction in the escape rate of the planet (only a factor of 2.5% of the value obtained in their other simulations). We believe such a simulation performed by Shaikhislamov et al. (2020) falls in our partially-open scenario (middle panels in Figure 5).

Although we did not model the π Men system, in the present work, we also found that the stellar wind might not necessarily lead to a significant reduction in escape rate, agreeing with Shaikhislamov et al. (2020). Nevertheless, when looking at the whole pa-

rameter space covered in our simulations, we found reduction in evaporation rates of up to 65% for the HJ simulations and 40% for the WN simulations. However, more importantly, we also found that this reduction is not linearly related to the depth of Ly- α transits – even when the escape rate is not substantially reduced, the absorption signature of escaping atmosphere can be significantly affected. This is because the stellar wind confinement can change the volume of the absorbing material, without affecting too much the planetary escape rate.

5.2 Model limitations

The aim of this work was to study in a systematic way how the stellar wind could affect atmospheric escape rates and how this would be observed in synthetic transits. Our model is relatively fast to run – roughly, a simulation takes about 8h to compute in 40 processors, although it could take longer in some cases. This enabled us to model nearly 30 different physical setups. However, our model can still be improved. For example, our 3D simulations model the flow of ionised hydrogen. They are isothermal and ignore the effects of magnetic fields, radiation pressure and charge exchange.

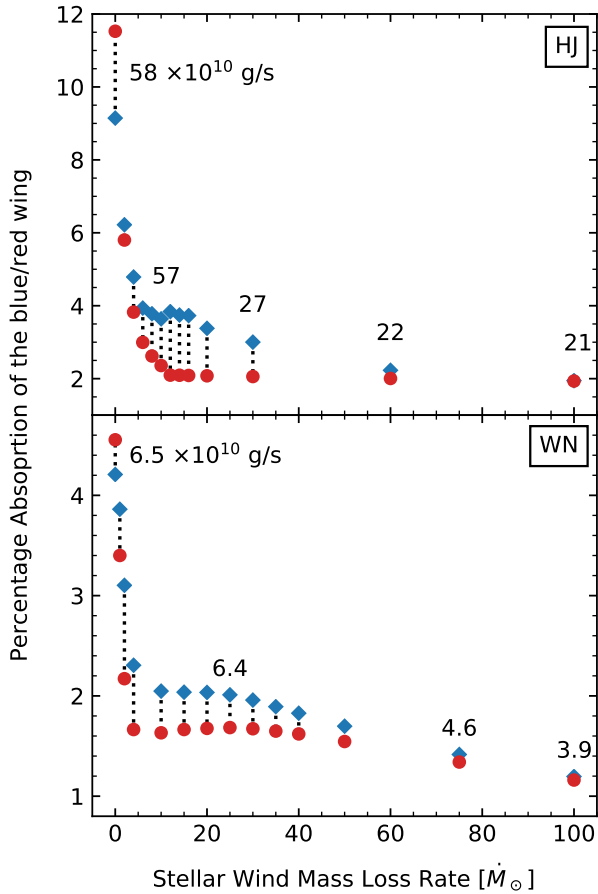


Figure 8. The percentage absorption in the blue (blue diamonds, -300 to -40 km/s) and red (red circles, 40 to 300 km/s) wings of Ly- α line as the stellar wind mass-loss rate is increased. The dotted line links points from the same model. The top panel shows the results for the HJ model while the bottom shows the WN models. At various points the atmospheric escape rate of the planet is marked in units of 10^{10} g/s.

A caveat of the 3D isothermal model is that we cannot match both the ram pressure and sonic point found in the 1D model². In this work, we chose to match the ram pressure of the escaping atmospheres, and as a result obtain sonic surfaces that are much closer to the planet than that predicted in the 1D model. To investigate how matching the sonic point would affect our results, we run one additional model of the WN planet in a $100 M_{\odot}$ stellar wind, ensuring that the sonic point remains at the same position as the 1D model, ie., at $1.9 r_p$. This was done by reducing the temperature of the outflow from 5000 to 3100K, resulting in a sonic point that is further out, and a lower velocity outflow. We chose a base density such that escape rate for this model with no stellar wind matches that of the previous version, 6.5×10^{10} g/s. When the $100 M_{\odot}$ stellar wind is injected into this model, we find that the atmospheric escape rate is reduced further than in the original, to 2.2×10^{10} g/s (previously 3.9×10^{10} g/s). This confirms that the larger the sonic point distance, the easier a stellar wind can disrupt this surface, and a greater reduction in escape rate will be found. However it

² It is a coincidence that the sonic point in the HJ simulation is at a similar distance in the 1D and 3D models

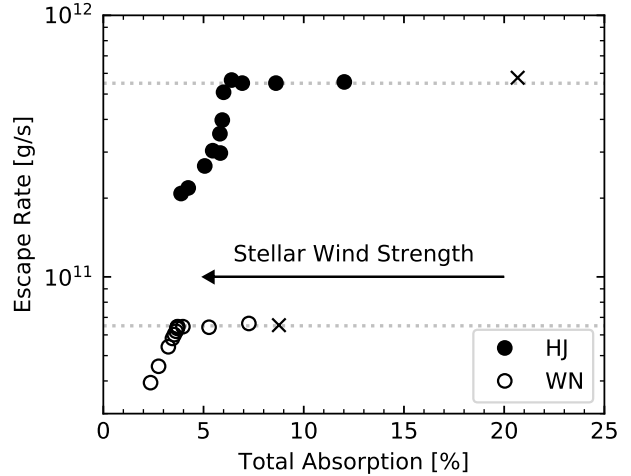


Figure 9. Atmospheric escape rate as a function of the percentage absorption of the blue+red wings of the Ly- α line at mid transit. The filled and open circles represent the HJ and WN models, respectively. For each set of models, we see a region where, although the escape rate is constant (marked with dotted lines), the transit absorption is not. The points marked with x are the models of each planet with no stellar wind, and from right to left, the stellar wind strength is increases (marked with an arrow).

also places importance on advancing our 3D model, as although we have now matched the sonic point, the ram pressure of the outflow is lower than found in the 1D model. This lower ram pressure provides less resistance against the incoming stellar wind, which when accompanied by the higher sonic point means the stellar wind can more easily disrupt the inner regions of the escaping atmosphere and affect the escape rate.

Carroll-Nellenback et al. (2017) showed using 3D hydrodynamics simulations that the sonic surface of the escaping atmosphere is significantly different when assuming an isotropic versus an anisotropic temperature distribution at the planetary boundary (their anisotropic model mimics a nightside of the planet). This obviously has implications on the atmospheric escape rate, with the anisotropic models of Carroll-Nellenback et al. (2017) showing an escape rate that was approximately 50% lower compared to the isotropic models. Temperature differences arise naturally in 3D models that solve for the radiative transfer of stellar photons through the planetary atmosphere (e.g. Debrecht et al. 2019). Although the day-night temperature differences are important to model, as they affect the planetary escape rate, we nevertheless expect that the hydrodynamic effects of the stellar wind on atmospheric escape is overall consistent to what we modeled here.

The presence of planetary magnetic fields, not included here, should also affect atmospheric escape. Owen & Adams (2014) demonstrated that magnetised exoplanets lose a factor of 4 to 8 times less mass than unmagnetised planets. This is because only a fraction of magnetic field lines around the planet remains open, along which ionised flows can escape. Khodachenko et al. (2015) found that a dipolar magnetic field of 1G around a HD209458b-analog planet was capable of reducing mass loss by up to an order of magnitude. Additionally, in the case of a magnetised planet, the planetary magnetic field can deflect the stellar wind (e.g. Carolan et al. 2019), which might no longer directly access the upper atmosphere of the planet. There has been recent debate in the literature discussing whether a planet's magnetic field can prevent atmospheric erosion

or could increase atmospheric losses (Blackman & Tarduno 2018). On one hand, the stellar wind is believed to erode atmospheres of unmagnetised planets, as is believed was the case of the young Mars, which was embedded in a much stronger young solar wind (Kulikov et al. 2007). On the other hand, the similar present-day ion escape rates of Mars, Venus and Earth have been used as counter-examples of planets that have very different magnetic field structures and yet present similar escape rates (Strangeway et al. 2010). There are still several unanswered questions on how the magnetic field of a close-in exoplanet could affect atmospheric escape and transit signatures.

Finally, our model neglects two physical processes, namely radiation pressure and charge exchange, both of which have been suggested to produce the population of neutral atoms that absorbs in the wing of Ly- α at high blue-shifted velocities (~ 100 km/s). Radiation pressure has been proposed to cause the acceleration of neutral hydrogen to speeds required to reproduce what is seen in Ly- α transits (Bourrier et al. 2015; Schneiter et al. 2016). However, radiation pressure alone might not be as significant (Debrecht et al. 2020). Another alternative is that charge exchange processes could produce high-velocity neutral hydrogen (Holmström et al. 2008; Kislyakova et al. 2014; Bourrier et al. 2016; Tremblin & Chiang 2013; Shaikhislamov et al. 2016), with a combination of charge exchange and radiation pressure processes best explaining observations of HD209468b (Esquivel et al. 2019). Though both of these effects can yield more high velocity hydrogen and thus affect the observational characteristics of the system, they are not thought to affect the inner regions of the escaping atmosphere. Charge exchange happens mostly around the shock, as one needs stellar wind protons interacting with neutrals from the planet's atmosphere (Shaikhislamov et al. 2016). Radiation pressure could affect the outer layers of the planetary atmosphere, but gets absorbed as they penetrate the atmosphere (self-shielding). Due to this they are unlikely to significantly change the hydrodynamics of the planetary outflow though may contribute to the obtained transit line profile (Cherenkov et al. 2018). For these reasons, we do not expect them to contribute to the disruption of the sonic surface that we study with our models.

6 CONCLUSIONS

We have seen significant progress in modeling atmospheric escape in close-in planets over the past two decades (Lammer et al. 2003; Murray-Clay et al. 2009; Bourrier & Lecavelier des Etangs 2013; Villarreal D'Angelo et al. 2018; Debrecht et al. 2020). However, many current models still neglect the interaction of the planet's upper atmosphere with the wind of the host stars. In particular, 1D hydrodynamic escape models are unable to treat the presence of the stellar wind – for that, multi-dimensional simulations are required. It has been demonstrated that the wind of the host star can affect atmospheric escape in exoplanets (Matsakos et al. 2015; Shaikhislamov et al. 2016; Villarreal D'Angelo et al. 2018; McCann et al. 2019; Vidotto & Cleary 2020). However, one of the open questions is currently for which systems the stellar wind would mostly affect atmospheric escape. One particular issue is that we do not have a full picture of how winds of cool dwarf stars vary from star to star. Cool dwarf stars are the most commonly known planet-hosts, but their winds are difficult to probe, with only a few techniques currently providing stellar wind measurements (e.g. Wood et al. 2005; Vidotto & Donati 2017; Fichtinger et al. 2017; Jardine & Collier Cameron 2019).

In this work, we systematically examined the effects of stellar winds on planetary atmospheric escape to determine whether and

when neglecting the presence of the stellar wind is justified. We used 3D hydrodynamic simulations to model the planetary outflowing atmosphere interacting with the stellar wind, which was injected in the simulation domain by means of an outer boundary condition. We performed this study on two different gas giant planets, a Hot Jupiter similar to HD209458b but orbiting a more active star (HJ) and a Warm Neptune similar to GJ3470b (WN), and varied the stellar wind mass-loss rate from 0 to $100\dot{M}_\odot$, where $\dot{M}_\odot = 2 \times 10^{-14} M_\odot/\text{yr}$ is the present-day solar mass-loss rate. In total, we performed nearly 30 3D hydrodynamics simulations of these systems.

For both planets, we found that as the stellar wind mass-loss rate was increased the planetary outflow was confined closer to the planet. As this confinement moved closer to the planet, planetary material could not properly accelerate, which eventually inhibited the dayside outflow from reaching super-sonic speeds. The inner regions of the escaping atmosphere were then affected, causing a reduced escape rate. For the HJ planet, the escape rate was reduced from $5.8 \times 10^{11} \text{ g/s}$, when no stellar wind was considered, to $2.1 \times 10^{11} \text{ g/s}$, when a wind with $100\dot{M}_\odot$ was considered. For the WN model, the planetary escape rates varied from $6.5 \times 10^{10} \text{ g/s}$ (no stellar wind) to $3.9 \times 10^{10} \text{ g/s}$ (strongest wind).

This reduction happened more suddenly in the HJ models than in the WN models, which we proposed is related to the distance of the sonic point. As the stellar wind strength increases, the escaping atmosphere is confined closer to the planet. This eventually disturbs the sonic surface of the outflowing atmosphere, transitioning from a "closed" to an "open" sonic surface configuration as seen in figure 5. This is ultimately what reduces the escape rate of the planet's atmosphere, as the stellar wind now interacts with a subsonic planetary outflow and prevents an outflow from fully developing (Christie et al. 2016; Vidotto & Cleary 2020). As the sonic point in the HJ models is further from the planet, the stellar wind can more easily affect it, so we see the escape rate of the HJ planet change over a short range in \dot{M} . In the WN planet, the sonic surface is very close to the planet. The stellar wind must now confine the escaping atmosphere much closer to the planet for the sonic surface to be affected, which results in a much more gradually transition from "closed" to "open" sonic surfaces in these models.

Using a ray-tracing technique, we investigated the possible observational signatures of this escape rate reduction in Ly- α transits. We found significant asymmetry towards the blue wing at mid-transit, which is to be expected when the day-side (redshifted) material is suppressed, and more material is funneled towards the planetary comet-like tail. This happens in the cases with larger stellar wind mass-loss rates. In the scenarios where only a weak wind (or no wind) were considered, the absorption in the red wing of the Ly- α line was larger, as some planetary material flows towards the star.

We also found that the changes caused in the atmospheric escape rate by the stellar wind affects Ly- α transits in a non-linear way. Across our set of models, the escape rate of the HJ planet was reduced from by 65% with the Ly- α absorption changing from 20.7 to 3.9%. For the WN planet, the escape rate was reduced by 40%, with a corresponding change in Ly- α absorption from 8.8% to 2.4%. However above 14% absorption in the HJ set (5% in the WN set) despite the percentage absorption changing significantly the atmospheric escape rate does not. These models represent the "closed" sonic surface models, where despite the volume of absorbing material changing, the sonic surface remains unaffected and so the escape rate does not vary. We concluded that the same atmospheric escape rate can therefore produce a range of absorptions depending on the strength of the stellar wind.

Neglecting the stellar wind when interpreting Ly- α observations can also lead to under-estimations of the planet's atmospheric escape rate. An unconfined escaping atmosphere can occupy a larger volume around the planet, and so a lower escape rate is required to produce significant absorption. Contrary to this, if the escaping atmosphere is confined by a strong stellar wind, a higher escape rate can produce the same absorption as the unconfined scenario, as the density of absorbing material increases. These degeneracies emphasise the importance of considering the stellar wind when interpreting transmission spectroscopic transits, in order to accurately estimate the atmospheric escape rate.

ACKNOWLEDGEMENTS

We thank the referee for their constructive review of this manuscript. This project has received funding from the European Research Council (ERC) under the European Union's Horizon 2020 research and innovation programme (grant agreement No 817540, ASTROFLOW). The authors wish to acknowledge the SFI/HEA Irish Centre for High-End Computing (ICHEC) for the provision of computational facilities and support. This work used the BATS-R-US tools developed at the University of Michigan Center for Space Environment Modeling and made available through the NASA Community Coordinated Modeling Center. CVD acknowledge the funding from the Irish Research Council through the postdoctoral fellowship (Project ID: GOIPD/2018/659).

DATA AVAILABILITY

The data described in this article will be shared on reasonable request to the corresponding author.

REFERENCES

Allan A., Vidotto A. A., 2019, MNRAS, 490, 3760

Baraffe I., Selsis F., Chabrier G., Barman T. S., Allard F., Hauschildt P. H., Lammer H., 2004, A&A, 419, L13

Beaugé C., Nesvorný D., 2013, ApJ, 763, 12

Ben-Jaffel L., Ballester G. E., 2013, A&A, 553, A52

Berger T. A., Huber D., Gaidos E., van Saders J. L., Weiss L. M., 2020, arXiv e-prints, p. arXiv:2005.14671

Bisikalo D., Kaygorodov P., Ionov D., Shematovich V., Lammer H., Fossati L., 2013, ApJ, 764, 19

Blackman E. G., Tarduno J. A., 2018, MNRAS, 481, 5146

Bourrier V., Lecavelier des Etangs A., 2013, A&A, 557, A124

Bourrier V., Ehrenreich D., Lecavelier des Etangs A., 2015, A&A, 582, A65

Bourrier V., Lecavelier des Etangs A., Ehrenreich D., Tanaka Y. A., Vidotto A. A., 2016, A&A, 591, A121

Bourrier V., et al., 2018, A&A, 620, A147

Carolan S., Vidotto A. A., Loesch C., Coogan P., 2019, MNRAS, 489, 5784

Carroll-Nellenback J., Frank A., Liu B., Quillen A. C., Blackman E. G., Dobbs-Dixon I., 2017, MNRAS, 466, 2458

Cherenkov A. A., Bisikalo D. V., Kosovichev A. G., 2018, MNRAS, 475, 605

Christie D., Arras P., Li Z.-Y., 2016, ApJ, 820, 3

Debrecht A., Carroll-Nellenback J., Frank A., McCann J., Murray-Clay R., Blackman E. G., 2019, MNRAS, 483, 1481

Debrecht A., Carroll-Nellenback J., Frank A., Blackman E. G., Fossati L., McCann J., Murray-Clay R., 2020, MNRAS, 493, 1292

Dong C., Jin M., Lingam M., Airapetian V. S., Ma Y., van der Holst B., 2018, Proceedings of the National Academy of Science, 115, 260

Edson A., Lee S., Bannon P., Kasting J. F., Pollard D., 2011, Icarus, 212, 1

Ehrenreich D., et al., 2015, Nature, 522, 459

Esquivel A., Schneiter M., Villarreal D'Angelo C., Sgró M. A., Krapp L., 2019, MNRAS, 487, 5788

Fichtinger B., Güdel M., Mutel R. L., Hallinan G., Gaidos E., Skinner S. L., Lynch C., Gayley K. G., 2017, A&A, 599, A127

Fulton B. J., et al., 2017, AJ, 154, 109

García Muñoz A., Youngblood A., Fossati L., Gandolfi D., Cabrera J., Rauer H., 2020, ApJ, 888, L21

Holmström M., Ekenbäck A., Selsis F., Penz T., Lammer H., Wurz P., 2008, Nature, 451, 970

Jardine M., Collier Cameron A., 2019, MNRAS, 482, 2853

Jensen A. G., Redfield S., Endl M., Cochran W. D., Koesterke L., Barman T., 2012, ApJ, 751, 86

Jia X., Kivelson M. G., 2016, Journal of Geophysical Research (Space Physics), 121, 1413

Jia X., Slavin J. A., Gombosi T. I., Daldorff L. K. S., Toth G., Holst B., 2015, Journal of Geophysical Research (Space Physics), 120, 4763

Johnstone C. P., et al., 2015, ApJ, 815, L12

Kasting J. F., Whitmire D. P., Reynolds R. T., 1993, Icarus, 101, 108

Kavanagh R. D., et al., 2019, MNRAS, 485, 4529

Khodachenko M. L., Shaikhislamov I. F., Lammer H., Prokopov P. A., 2015, ApJ, 813, 50

Khodachenko M. L., Shaikhislamov I. F., Lammer H., Berezutsky A. G., Miroshnichenko I. B., Rumenskikh M. S., Kislyakova K. G., Dwivedi N. K., 2019, ApJ, 885, 67

Kislyakova K. G., et al., 2014, A&A, 562, A116

Kubyshkina D., Vidotto A. A., Fossati L., Farrell E., 2020, MNRAS, 499, 77

Kulikov Y. N., Lammer H., Lichtenegger H. I. M., Penz T., Breuer D., Spohn T., Lundin R., Biernat H. K., 2007, Space Sci. Rev., 129, 207

Kulow J. R., France K., Linsky J., Loyd R. O. P., 2014, ApJ, 786, 132

Kurokawa H., Nakamoto T., 2014, ApJ, 783, 54

Lammer H., Selsis F., Ribas I., Guinan E. F., Bauer S. J., Weiss W. W., 2003, ApJ, 598, L121

Lampón M., et al., 2020, A&A, 636, A13

Lecavelier Des Etangs A., et al., 2010, A&A, 514, A72

Lecavelier des Etangs A., et al., 2012, A&A, 543, L4

Lingam M., Loeb A., 2018, International Journal of Astrobiology, 17, 116

Ma Y., Russell C. T., Nagy A. F., Toth G., Dong C., Bouger S. W., 2013, AGU Fall Meeting Abstracts, pp P13C-05

Manchester W. B., Gombosi T. I., Roussev I., Ridley A., De Zeeuw D. L., Sokolov I. V., Powell K. G., Tóth G., 2004, J. Geophys. Res.~(Space Physics), 109, 2107

Matsakos T., Uribe A., Königl A., 2015, A&A, 578, A6

Mazeh T., Holczer T., Faigler S., 2016, A&A, 589, A75

McCann J., Murray-Clay R. A., Kratter K., Krumholz M. R., 2019, ApJ, 873, 89

Murray-Clay R. A., Chiang E. I., Murray N., 2009, ApJ, 693, 23

Oklopčić A., Hirata C. M., 2018, ApJ, 855, L11

Owen J. E., Adams F. C., 2014, MNRAS, 444, 3761

Owen J. E., Lai D., 2018, MNRAS, 479, 5012

Parker E. N., 1958, ApJ, 128, 664

Pillitteri I., Maggio A., Micela G., Sciortino S., Wolk S. J., Matsakos T., 2015, ApJ, 805, 52

Schneiter E. M., Esquivel A., Villarreal D'Angelo C. S., Velázquez P. F., Raga A. C., Costa A., 2016, MNRAS, 457, 1666

Shaikhislamov I. F., et al., 2016, ApJ, 832, 173

Shaikhislamov I. F., Fossati L., Khodachenko M. L., Lammer H., García Muñoz A., Youngblood A., Dwivedi N. K., Rumenskikh M. S., 2020, arXiv e-prints, p. arXiv:2006.06959

Sterenborg M. G., Cohen O., Drake J. J., Gombosi T. I., 2011, Journal of Geophysical Research (Space Physics), 116, A01217

Strangeway R. J., Russell C. T., Luhmann J. G., Moore T. E., Foster J. C., Barabash S. V., Nilsson H., 2010, AGU Fall Meeting Abstracts, Tóth G., et al., 2005, Journal of Geophysical Research (Space Physics), 110, A12226

Tremblin P., Chiang E., 2013, MNRAS, 428, 2565

Vidal-Madjar A., Lecavelier des Etangs A., Désert J. M., Ballester G. E., Ferlet R., Hébrard G., Mayor M., 2003, *Nature*, 422, 143

Vidotto A. A., Cleary A., 2020, *MNRAS*, 494, 2417

Vidotto A. A., Donati J. F., 2017, *A&A*, 602, A39

Vidotto A. A., et al., 2018, *MNRAS*, 481, 5296

Villarreal D'Angelo C., Esquivel A., Schneiter M., Sgró M. A., 2018, *MNRAS*, 479, 3115

Weber E. J., Davis Jr. L., 1967, *ApJ*, 148, 217

Wood B. E., Müller H. R., Zank G. P., Linsky J. L., Redfield S., 2005, *ApJ*, 628, L143

Yelle R. V., 2004, *Icarus*, 170, 167

Zank G. P., Müller H. R., 2003, *Journal of Geophysical Research (Space Physics)*, 108, 1240

van der Holst B., et al., 2011, *ApJS*, 194, 23